

# *Mechanical and electrical design of a biped humanoid which has multiple motors on each lower body joint*

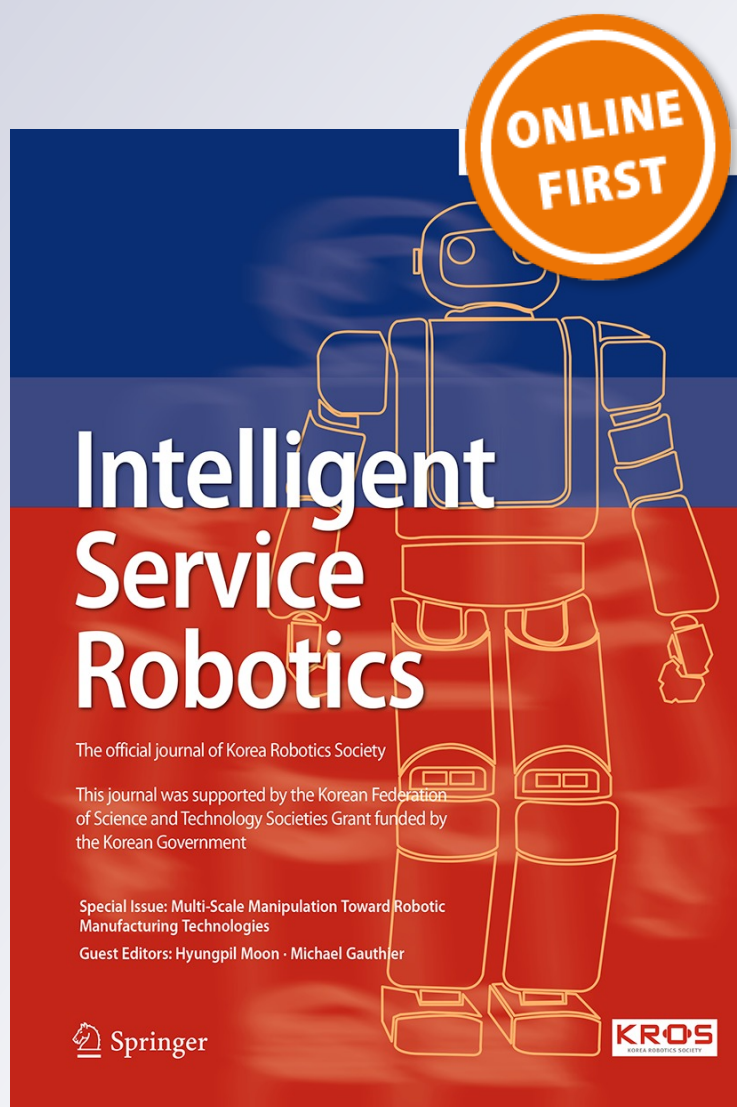
**Sunwoo Lee & Ill-Woo Park**

**Intelligent Service Robotics**

ISSN 1861-2776

Intel Serv Robotics

DOI 10.1007/s11370-015-0184-z



**Your article is protected by copyright and all rights are held exclusively by Springer-Verlag Berlin Heidelberg. This e-offprint is for personal use only and shall not be self-archived in electronic repositories. If you wish to self-archive your article, please use the accepted manuscript version for posting on your own website. You may further deposit the accepted manuscript version in any repository, provided it is only made publicly available 12 months after official publication or later and provided acknowledgement is given to the original source of publication and a link is inserted to the published article on Springer's website. The link must be accompanied by the following text: "The final publication is available at [link.springer.com](http://link.springer.com)".**

# Mechanical and electrical design of a biped humanoid which has multiple motors on each lower body joint

Sunwoo Lee<sup>1</sup> · Ill-Woo Park<sup>1</sup>

Received: 27 January 2015 / Accepted: 20 July 2015  
© Springer-Verlag Berlin Heidelberg 2015

**Abstract** The design of a biped humanoid that has multiple motors on each lower body joint is described. The joint actuators of the lower body should have high-power performance with compact size for walking while dynamically supporting the entire weight. The authors propose a design method in which multiple motors are installed in a joint. The method can amplify the joint torque and this is verified by experiments involving measurement of the joint angle and the current with respect to the number of motors on a single joint. The mechanical design and control system are explained. The design results are verified from a walking experiment. The proposed design improved the walking performance.

**Keywords** Biped locomotion · Biped walking robot · Control hardware design · Humanoid · Robot design

## 1 Introduction

A fully actuated biped walking robot, in contrast to a passive walking robot [1], uses active actuators in all the joints of the lower body [2–6]. The Wabian-2 (41 degrees of freedom (DoF), size 1.53 m, mass 64.5 kg) was developed at Waseda University [3]. It has seven DoF in each leg and two DoF in the upper body. The Honda Motor Corporation developed ASIMO-R, which has 34 DoF, 1.3 m height, and a weight of 54 kg. It can run at a maximum speed of 6 km/h. In 2009, Honda published some details of the walking and running capability of ASIMO in [4]. The National Institute of Advanced Industrial Science and Technology (AIST) and

Kawada Industries developed HRP-3, which is 1.61 m tall, has a weight of 68 kg, and has 42 DoF. CAN communication is used for controlling the robot [5]. Beijing Institute of Technology developed a humanoid robot, named BHR-5 [6], which is an upgraded version of BHR-3. Samsung Advanced Institute of Technology developed human size humanoids named Mahru III [7] and Roboray [8]. They, respectively, have a single motor on each joint.

The University of Tokyo developed a life-size humanoid with a high-output actuation system. A water-cooled double motor is used as an actuation system of the robot on the hip and knee pitch joint [9]. The Korea Advanced Institute of Science and Technology (KAIST) developed HUBO, with a weight of 56 kg and height of 1.25 m. It also uses CAN communication for controlling motors and sensors. The robot used double motors on knee pitch joint [10]. The HUBO series robots are presented in [11] including the latest version of HUBO, HUBO2. The Hubo2 Plus robot is a 130 cm tall, 42 kg full-size humanoid that can run 3.6 km/h [12]. The robot's joint power is amplified by installing two motors on specific joints.

Harmonic drive reduction gears were used in all of the fully actuated humanoids in the above studies, because they have almost zero backlashes. The harmonic drive also has a large reduction gear ratio. For fast rotation of the output joint against the gear ratio (50:1–160:1) [13], the maximum speed of the motor should be relatively higher than the speed of the direct drive for flat type or pancake type motors [14]. The fast motors also have a relatively small torque specification (50–180 mNm). The maximum speed of generally used motors is about 6000–17,000 rpm. These types of motors have a tendency to have a small diameter and long length to make the rotor inertia small. Also, if a more powerful motor is needed, longer motors are required. This presents an exterior design problem of a wide leg in the frontal view. In this

✉ Ill-Woo Park  
mrquick@kw.ac.kr

<sup>1</sup> Kwangwoon University, Seoul, Korea

paper, the authors propose a method to enhance the actuator torque while maintaining the size by installing multiple high-speed motors in parallel on each leg joint. This paper presents experimental results demonstrating the power improvement of the joint and walking performance.

A humanoid is developed, with a height of 130 cm and a weight of 54 kg, to realize this idea. In the following sections, the robot's mechanical design, the electrical design of the motor controller and driver, the system integration, and the walking results for verification are explained. The robot design concept is explained in Sect. 2. The mechanical design of lower body which has multiple motors on each joint is presented in Sect. 3. To drive the motors, Sect. 4 gives the design result of motor controller and driver. Section 5 is about the sensor system of the humanoid robot which includes inertia measurement unit and loadcells. The result of system integration design is presented in Sect. 6. In comparison with [15, 16], which basically studied automatic gait generation, a stable walking trajectory and a feedback control algorithm are explained in Sect. 7. They are adopted from the research of [17–19] and [20–22], respectively, to realize stable biped walking. The Sect. 8 is dedicated to the walking experiment. The conclusion is presented in Sect. 9.

## 2 Robot design concept

In this section, the concepts and objectives of the robot design are introduced. There are four design concepts as follows:

- (i) Amplifiable joint power
- (ii) Negligible uncertainty
- (iii) Self-contained system
- (iv) Simple kinematics.

### 2.1 Amplifiable joint power

A robot joint actuator is always required to have compact size, fast speed, high torque, and light weight. The power per weight of the joint motor is important, because the joint should support the whole body's gravity force on the supporting phase of walking and its performance is evaluated by the walking speed. In the designing stage of a robot, its task should be defined first, because the robot's motion and the inertia of the work piece are the given conditions in designing the robot. For a biped humanoid, walking is a critical task. The desired walking performance depends not only on the joint actuator but also the stabilization and motion generation algorithm. With advances in this algorithm, higher performance of the joint actuator is required. It is inefficient, however, to design a new biped robot whenever such advances are made. Therefore, by designing a joint actuator that is easily upgradable, the time and cost of building a

robot will be saved. In this paper installing motors in parallel is proposed as a means of increasing the joint power.

### 2.2 Negligible uncertainty

The major joints such as all the joints of the legs should be robust. In other words, the output side of the joint should have zero uncertainty such as backlash. This is the reason why harmonic drive reduction gears are used in the joints. Moreover, the motor drive units such as motor controllers and drivers are mounted close to the actuators to reduce cable noise. If actuator uncertainty is allowed, it could destabilize the robot. The effect of uncertainty increases with the length of links.

### 2.3 Self-contained system

The main controller, motor control units, sensor units, and batteries are installed on the robot to accomplish untethered walking. The robot should be able to be operated remotely through wireless LAN.

### 2.4 Simple kinematics

The robot joints have been designed to have simple kinematics. By intersecting the joint axes, a simple closed form inverse kinematics solution exists. In this solution, trigonometric functions such as sine and cosine are involved, but no Jacobean inverse is involved. Therefore, path generation and controller design become simple and the uncertainty of numerical iteration is rejected. This point is related with the concept of zero uncertainty.

## 3 Mechanical design of lower body

The A schematic diagram of the lower body and its coordinate system are shown in Fig. 1. The configuration of the actuators for a leg is presented in Table 1. The joint power and torque are calculated by the approach of [23]. Fifteen motors are used in each leg for actuating 6 DoF joints.

### 3.1 Joint actuator design

Except the yaw joint in the hip, which is driven by a pulley–belt mechanism, the joint actuators are composed of a harmonic drive, multiple BLDC motors, and spur gears connecting the motor shafts and the harmonic drive's input, as shown in Figs. 2 and 3. The same motors are connected in parallel, and the input torque and the power of the Harmonic Drive are amplified as a result, in proportion to the number of inserted motors. The motor is selected to have fast speed, because adding motors in parallel cannot increase the speed.



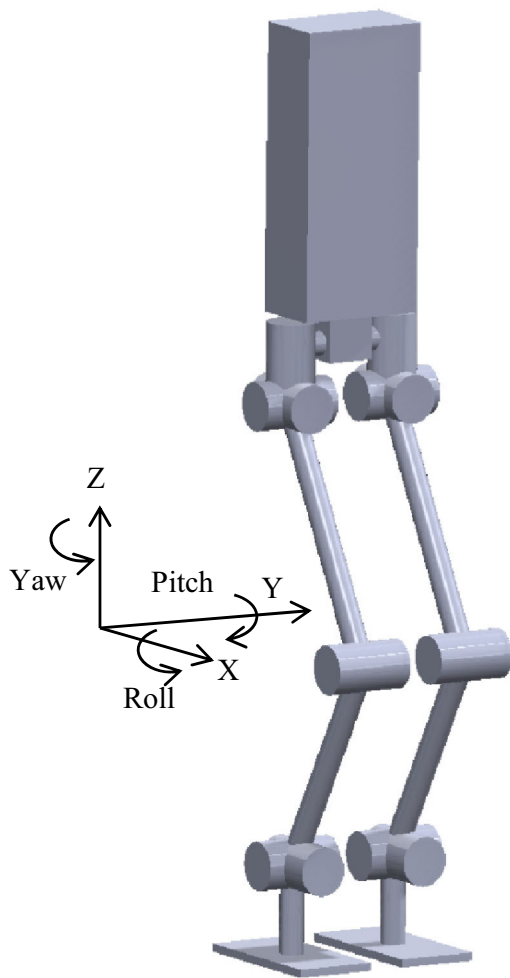


**Fig. 1** Schematic of lower body mechanical design and its coordinate system

**Table 1** Leg joint actuator configuration in each leg

Joint axis	Number of motors	Gear reduction ratio	Harmonic drive reduction ratio
<b>Hip</b>			
Yaw	1	4:1 <sup>a</sup>	100:1
Roll	2	7:1	120:1
Pitch	4	13:3	160:1
<b>Knee</b>			
Pitch	4	4:1	160:1
<b>Ankle</b>			
Pitch	2	13:3	160:1
Roll	2	7:1	120:1

<sup>a</sup> Pulley–belt connection between the motor and the Harmonic Drive's input

The intersecting rotation axes joints are designed as shown in Fig. 3. A hollow shaft harmonic drive is adopted because of the advantage it provides for wiring.

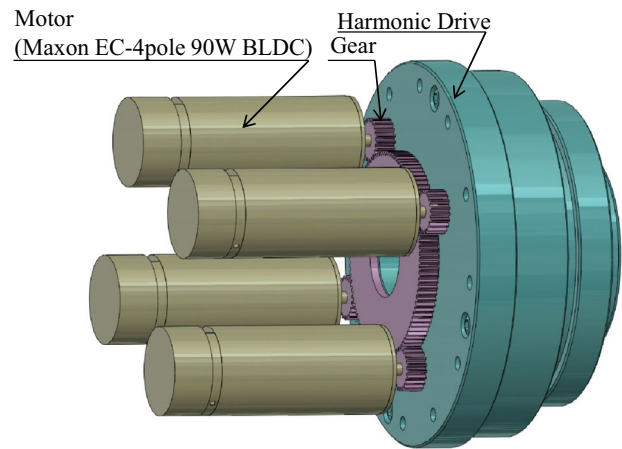


**Fig. 2** Mechanical design of multi-motor actuating single joint (knee joint)

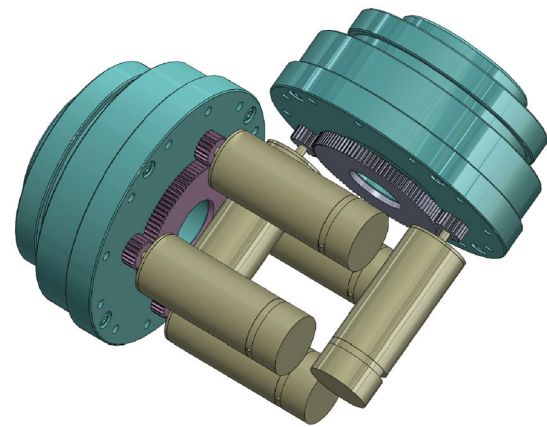


**Fig. 3** Mechanical design of a multiple motor actuating joint that has two intersecting rotation axes

### 3.2 Lower body design

The mechanical design is shown in Fig. 4. The lower body has 12 DoF. The joints in the hip and the ankle have intersecting rotation axes. There are 3 DoF in the hip joint, 1 DoF in the knee joint, and 2 DoF in the ankle joint on each leg. Considering the pelvis center of the torso as the base of the lower body's coordinate frame, the order of joint connection is yaw-roll-pitch in the hip, pitch in the knee, and pitch-roll in the ankle. The three rotation axes in the hip are designed such that they consecutively intersect at a point to provide a closed inverse kinematic solution. The axes in the ankle also intersect at a point to allow a simple kinematic solution.

In terms of leg size, the proposed method does not increase the width of the leg in the frontal view. The length of the motor is not increased by the parallel addition in its joint, as this only amplifies the torque and power. The main advantage of this method is that it allows robot design modification. The joint actuator power can be easily modified without mechanical

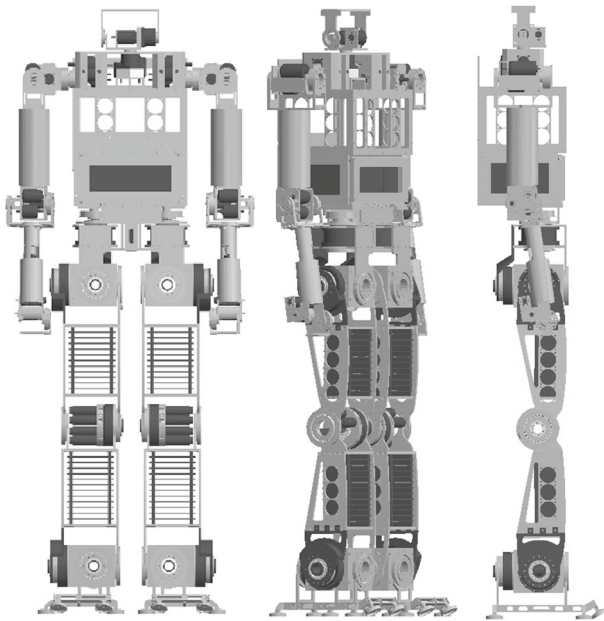


**Fig. 4** Mechanical design of the biped humanoid robot

redesign; i.e. the power can be amplified easily by inserting motors on a joint, keeping the motor's no load angular speed constant.

In the design stage of motor selection, the motor power per weight (P/W) is considered, because the method of installing multiple motors also increases the total weight of the motors. As an example, in the case of the EC-4pole Maxon motor, two 90 W motors are used to achieve an ideal 180 W and with an overall weight of 125 g. As a result, the P/W value is 0.75. When a single 200 W motor weighing 300 g is used, its P/W value is 0.67. In terms of the P/W, using two 90 W motors is better than using a single 200 W motor.

#### 4 Motor controller and driver design

The motor driver is designed using the 6-step BLDC trapezoidal control method. Its maximum power capability is

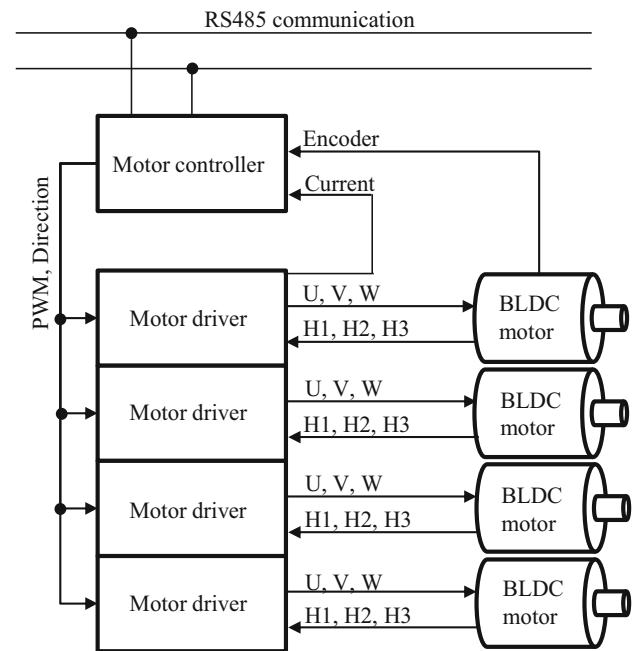
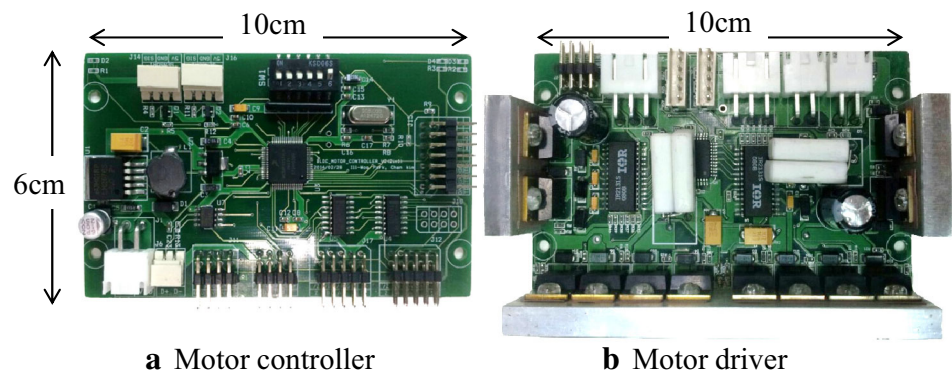


**Fig. 5** Schematic diagram of signal connection between motor controller, driver, and motor; H1, H2, and H3 are hall sensor signals

500 W/motor. The motor controller generates a pulse width modulation (PWM) signal as an input of the motor driver, as shown in Figs. 5 and 6. The PWM and the rotational direction signal pass through the electrically programmable logic device (EPLD), and 6 signals for driving the BLDC motor are generated with additional inputs of three hall sensor signals with BLDC commutation logic. Figure 6 shows the designed motor controller and driver.

The motor controller receives the PWM duty and direction commands from the main controller, as shown in Fig. 13, and returns the encoder position and current measurement data through RS485 communication, which is explained in Sect. 5. The overall current signal, in contrast with the concept of phase current, is measured by A/D (Analog to Digital) conversion of the signal of the current sensing resistor, which

**Fig. 6** Motor controller and BLDC motor driver board



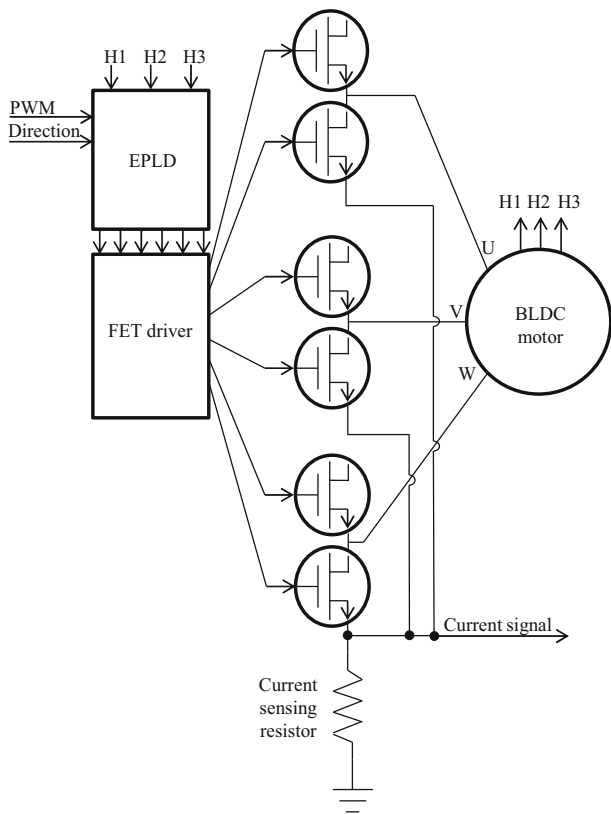


**Fig. 7** Schematic diagram of motor driver: H1, H2, and H3 are hall sensor signals

is shown in Fig. 7. For the multiple motors on a single joint, a decision problem of current measuring arises. In this paper, it is assumed that if the same motors on a joint are used, the overall currents of the motors are the same. One of the overall current signals of the multiple motor drivers for each motor is selected as a representative current signal of the joint actuator.

The joint control algorithm is executed on the main controller (PC) with a sampling frequency of 500 Hz. The control scheme of the joint motor is shown in Fig. 8. Basically, a position control scheme is used and current control is implemented on the inner loop. The current control of the motor is for over current limit control. The limit control is achieved by saturating the reference current, which is the output of the velocity control.

For a small value of PWM duty as an input, there is a non-responding zone of the motor current because the input voltage is in the cut-off region of the FET (Field Effect Transistor). In this case, the motor current cannot be measured; an almost “0” value is measured in the cut-off region. When the voltage increases from the cut-off region to the saturation region, the current value is abruptly measured near the cut-off region. This phenomenon introduces non-linearity of current control. The problem is solved using a signal mix-

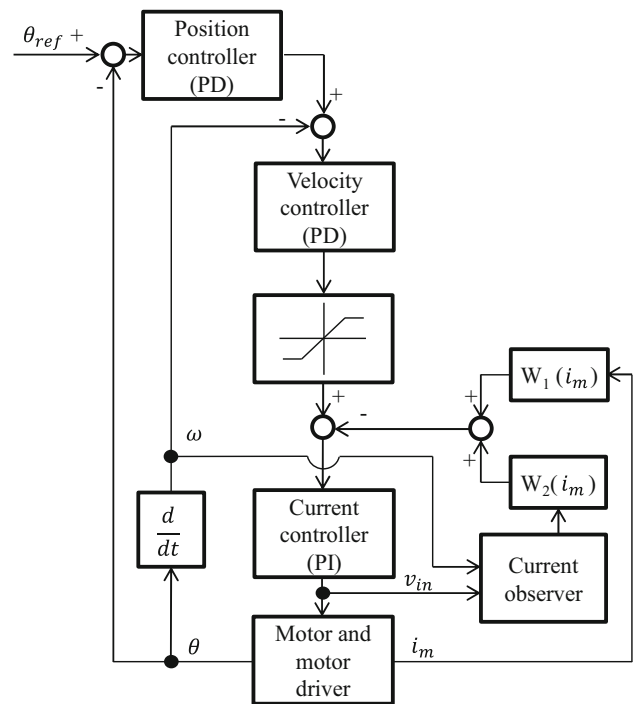


**Fig. 8** Motor control scheme :  $\theta_{ref}$  = reference position angle,  $\theta$  = actual position,  $i_m$  = measured current,  $v_{in}$  = input voltage, and  $W_1(i_m)$  and  $W_2(i_m)$  = weighting function

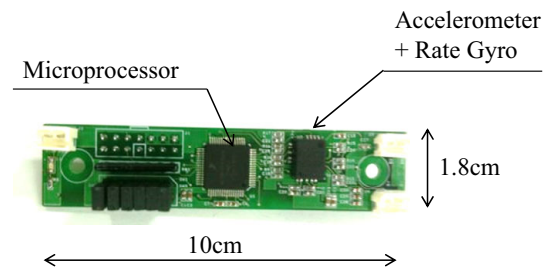


**Fig. 9** IMU (Inertial measurement unit)

ing algorithm by weighted summation ( $W_1(i_m)$  and  $W_2(i_m)$ ) with a closed-loop current observer and real measurement with respect to the magnitude of the input PWM duty, i.e. the input voltage. The weighting functions are the function of the measured current ( $i_m$ ). They are designed such that when  $i_m$  is small,  $W_1$  is decreases and  $W_2$  increases. The summation of weighting values is always 1.

## 5 Sensor system

Two kinds of sensors are installed. The first is an IMU (Inertial Measurement Unit), as shown in Fig. 9. It is attached on the center of the torso and the thighs of each leg. The sensor contains a 3-channel rate gyro, a 3-channel accelerometer, and a signal processor. The specifications are shown

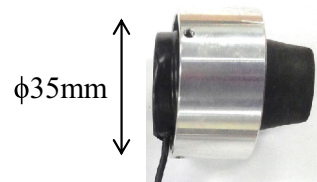
**Table 2** Specifications of IMU

Item	Unit	Value
Rate gyro		
Scale factor	mV/(°/s)	3.0
Range	°/s	±300
LPF bandwidth	Hz	200
Bias variation with temperature	mV	±24
Accelerometer		
Scale factor	mV/G	400
Range	G	±3
Bias variation with temperature	mG	±150

in Table 2. The walking control algorithms use the sensor actively. They are posture initialization, vibration reduction of the legs, and attitude control of the upper body. In practice, an accelerometer senses the inclination using an arcsine function. But it is very sensitive to unwanted acceleration such as shocks or jerks. On the other hand, a rate gyro is effective for sensing the angular velocity, but it drifts in low frequency. A complementary filter algorithm for processing the signal is, therefore, used to sense the robot's upper body posture. The IMUs, which are enclosed on the thighs, are employed for calculating the ZMP (Zero Moment Point) as an ancillary ZMP measure. The ZMP value can be directly measured by the load cell in this study.

The second sensor type is a load cell, as shown in Fig. 10. This sensor measures the reaction force from the ground in the vertical direction. It is installed at the four corners of each sole. Using the reaction forces, 2 axis torques (pitch and roll direction) and the ground normal force (Z direction) on each foot can be calculated. The ZMP is simply measured by dividing the torque by the normal force. In order to realize a stable walking algorithm, ground contact sensing of the sole, the ZMP, and the reaction ankle torque against the supporting ground are also needed. The sensor system is utilized for these algorithms.

**Fig. 10** Load cell and its signal processing board

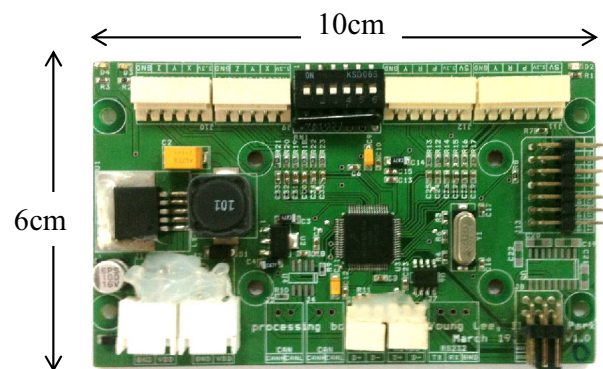


**a** Load cell

Figure 11 shows the top view of the left foot schematic as an example. The load cells are located on the four corners. Using this load cell placement, two moments ( $M_x$ ,  $M_y$ ) and one force ( $f$ ) can be measured, and these are the major signals used to calculate the ZMP. The load cells only measure the vertical direction forces, which are the forces of the ground reaction. The moments can be calculated as  $M_x^L = (f_1^L + f_2^L)d_1^L - (f_3^L + f_4^L)d_4^L$ ,  $M_y^L = (f_1^L + f_4^L)d_2^L - d_4^L(f_2^L + f_3^L)$  in left foot, and  $M_x^R = (f_1^R + f_2^R)d_1^R - (f_3^R + f_4^R)d_4^R$ ,  $M_y^R = (f_1^R + f_4^R)d_2^R - d_4^R(f_2^R + f_3^R)$  in right foot. The superscripts “L” and “R” mean left and right. The numbers in subscript mean the number of load cells in each foot. The normal forces on feet are  $f^L = f_1^L + f_2^L + f_3^L + f_4^L$  and  $f^R = f_1^R + f_2^R + f_3^R + f_4^R$ . Figure 12 is also a top view of the schematic of two feet for calculating the ZMP. The ZMP, on the basis of its physical meaning, is calculated by the summation of moments divided by the reaction force from the ground. Specifically, it can be calculated as  $x_{ZMP} = \frac{M_y^L + f^L x_L + M_y^R + f^R x_R}{f^L + f^R}$  and  $y_{ZMP} = \frac{M_x^L + f^L y_L + M_x^R + f^R y_R}{f^L + f^R}$ .

## 6 System integration

A schematic diagram of the hardware system is shown in Fig. 13, and a physical overview of the mechanical design result is shown in Fig. 14. The system contains 30 BLDC motors on legs (12 DoF), 12 DC motors on the arms (10 DoF) and head (2 DoF), 8 load cells on the soles (4/sole), and 3 inertial measurement units (IMU) (3 axis rate gyros and 3 axis accelerometers/unit) on the torso and thighs. For communication arbitration, 4 boards are connected with a 4-channel universal asynchronous receiver transmitter (UART) communication card, which is attached to the peripheral component interconnect express (PCIe) bus of the main controller.



**b** Signal processing board



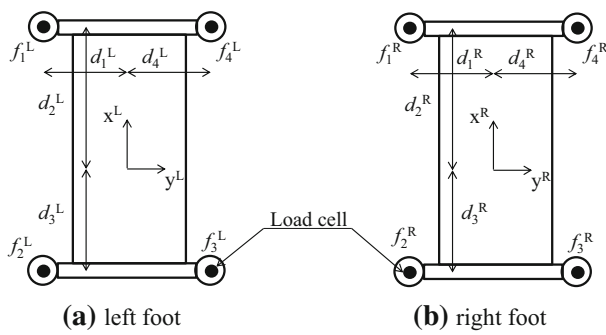


**Fig. 11** Top view of the foot and loadcell placement schematic

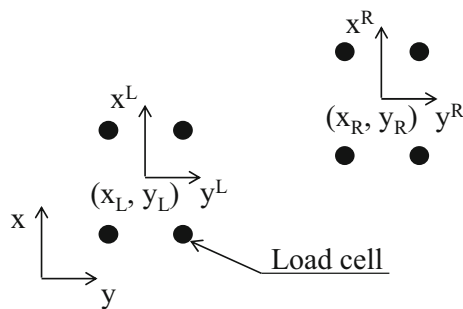


**Fig. 12** Top view of the feet schematic for calculating the ZMP

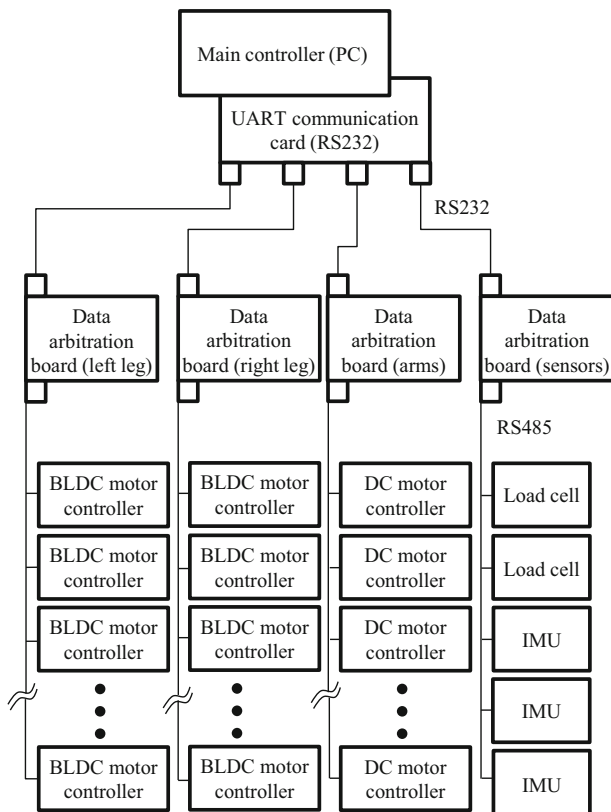


**Fig. 13** Schematic of hardware system integration

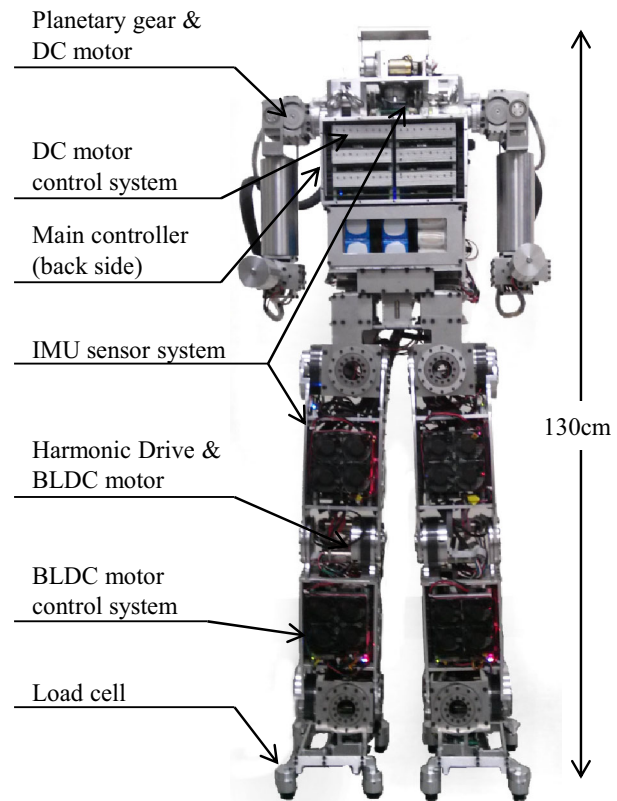


**Fig. 14** Robot system overview

The operating system (OS) of the main controller is Linux. For realizing real-time control, Xenomai is patched on the Linux kernel. The UART communication card, which uses PCIe (PCI Express Bus), driver is also developed for flexible communication packet design and for low signal latency in real time. All data for controlling the robot are transferred bi-directionally at a control frequency of 500 Hz. The communication system uses a full duplex RS232 and a half duplex RS485. The TTL level voltage of RS232 is used between the main controller and the data arbitration board. The board converts RS232 into RS485, and it optimizes the data packets to increase the efficiency of data transfer.

## 7 Walking trajectory

The modeling of the robot for stable trajectory generation is explained in this section [17–19] to realize the stable biped walking of the robot. A detailed explanation of stable walking trajectory generation can be found in [17], which presents the full mathematical equations and simulation results. The robot is modeled with a simple inverted pendulum model (SIPM). Figure 15 shows the SIPM with the sagittal and frontal view points.

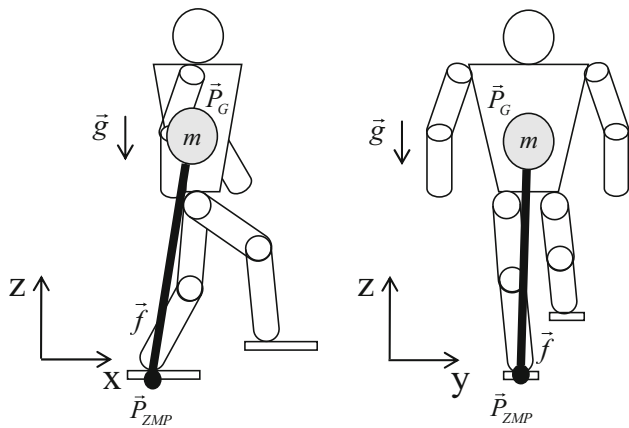


**Fig. 15** SIPM of robot ( $\vec{P}_G$  is the center of gravity position.  $\vec{P}_{ZMP}$  is ZMP.  $\vec{f}$  is reaction force from supporting ground.  $m$  is mass of the robot.  $\vec{g}$  is gravity acceleration)

### 7.1 SIPM for walking trajectory generation

The relation between the center of gravity (CoG) and the ZMP is given by Eq. (1) with this model. The equation uses the dynamic equation of the forces and the definition of the ZMP, which is the point where the total summation of moments is zero.

$$\begin{aligned} m(\ddot{\vec{P}}_G + \vec{g}) &= \vec{f} \\ (\vec{P}_G - \vec{P}_{ZMP}) \times \vec{f} &= 0, \end{aligned} \quad (1)$$

$$\begin{aligned} \text{where } \vec{P}_G &= [x_G \ y_G \ z_G]^T, \vec{g} = [0 \ 0 \ g]^T, \\ \vec{f} &= [f_x \ f_y \ f_z]^T, \vec{P}_{ZMP} = [x_{ZMP} \ y_{ZMP} \ 0]^T \end{aligned}$$

$$\begin{aligned} \ddot{x}_G &= \omega_G^2 (x_G - x_{ZMP}) \\ \ddot{y}_G &= \omega_G^2 (y_G - y_{ZMP}) \\ \omega_G^2 &= \frac{\ddot{z}_G + g}{z_G} \end{aligned} \quad (2)$$

The desired ZMP trajectory design is equivalent to  $\vec{P}_{ZMP}$  design and the ZMP should be located inside the supporting polygon. Equation (1) can be reformulated as (2) and we can then obtain (3) by simple modification:

$$\begin{aligned} x_G - \frac{1}{\omega_G^2} \ddot{x}_G &= x_{ZMP} \\ y_G - \frac{1}{\omega_G^2} \ddot{y}_G &= y_{ZMP} \end{aligned} \quad (3)$$

If the vertical movement of the robot is negligible,  $\omega_G$  is constant. And its physical meaning is natural frequency of pendulum. The ZMP trajectory can be designed without coordinate dependency in the  $x$  and  $y$  directions. The CoG,  $(x_G, y_G)$ , a trajectory generation problem, entails solving the

differential equation (3) after designing the ZMP trajectory,  $(x_{ZMP}, y_{ZMP})$ . We present the representative equation (4), with the observation that each equation in (3) has similar form,

$$\varphi - \frac{1}{\omega_G^2} \ddot{\varphi} = \mu, \quad (4)$$

where the  $\varphi$  and the  $\mu$  stand for  $\{x_G, y_G\}$ , and  $\{x_{ZMP}, y_{ZMP}\}$ , respectively.

### 7.2 Desired ZMP trajectory design and the CoG trajectory solution

This section briefly explains how to solve the CoG from the designed ZMP. Equation (5) shows that the desired ZMP trajectory can be designed by a finite Fourier series.

$$\mu(t) = \frac{a_0}{2} + \sum_{i=1}^M [a_i \cos(i\omega_0 t) + b_i \sin(i\omega_0 t)], \quad (5)$$

where  $M$  is the order of the Fourier series;  $a_0$ ,  $a_i$ , and  $b_i$  are the designed coefficients;  $\omega_0$  is the fundamental frequency.

The solution,  $\varphi(t)$ , has a homogeneous ( $\varphi_h(t)$ ) and a particular ( $\varphi_p(t)$ ) part. The relation of the coefficients can be easily derived as  $\alpha_0 = a_0$ ,  $\alpha_i = a_i(1 + (\frac{i\omega_0}{\omega_G})^2)^{-1}$  and  $\beta_i = b_i(1 + (\frac{i\omega_0}{\omega_G})^2)^{-1}$ .

$$\varphi_h(t) = \eta_1 \cosh(\omega_G t) + \eta_2 \sinh(\omega_G t) \quad (6)$$

$$\varphi_p(t) = \frac{\alpha_0}{2} + \sum_{i=1}^M [\alpha_i \cos(i\omega_0 t) + \beta_i \sin(i\omega_0 t)], \quad (7)$$

The design parameters for the desired ZMP trajectory are  $M$ , the coefficients  $a_0$ ,  $a_i$ , and  $b_i$ , and the fundamental frequency ( $\omega_0$ ) in each time segment. Eventually, solving the CoG trajectory involves finding the coefficients  $\eta_1$  and  $\eta_2$ .

After the desired ZMP trajectory is designed, a time segmentation scheme is used to describe the walking action in each step. The main issue of segmentation is solving the coefficients, which maintains the connectivity of the CoG trajectory between the segments. The desired ZMP and the CoG trajectories in the  $j$ -th ( $j = 1, 2, \dots, n$ ) time segment are expressed as follows:

$$\begin{aligned} \mu^{(j)}(t) &= \frac{a_0^{(j)}}{2} + \sum_{i=1}^{M^{(j)}} [a_i^{(j)} \cos(i\omega_0^{(j)}(t - t_{j-1})) \\ &\quad + b_i^{(j)} \sin(i\omega_0^{(j)}(t - t_{j-1}))] \\ \varphi^{(j)}(t) &= \eta_1^{(j)} \cosh(\omega_G(t - t_{j-1})) \\ &\quad + \eta_2^{(j)} \sinh(\omega_G(t - t_{j-1})) \end{aligned} \quad (8)$$

$$+ \frac{\alpha_0^{(j)}}{2} + \sum_{i=1}^{M^{(j)}} [\alpha_i^{(j)} \cos(i\omega_0^{(j)}(t - t_{j-1})) + \beta_i^{(j)} \sin(i\omega_0^{(j)}(t - t_{j-1}))], \quad (9)$$

where  $t_j$  is the end time in the  $j$ -th segment, and for this study,  $\omega_0^{(j)} = \pi/(2(t_j - t_{j-1}))$ .

The CoG trajectory contains the unknown coefficients  $\eta_1^{(j)}$  and  $\eta_2^{(j)}$  in each segment. They should be calculated to preserve the position and velocity connectivity on the start-end point of the segments. For  $n$  segments, there are  $2n$  unknowns. When the following conditions are used, the coefficients can be calculated: the initial condition, the position–velocity connectivity conditions, and the terminal condition of the CoG at the final time ( $t_n$ ).

*Initial condition*

When the initial condition  $\varphi^{(1)}(t_0)$  is given, (10) becomes

$$\begin{bmatrix} 1 & 0 \end{bmatrix} \begin{bmatrix} \eta_1^{(1)} \\ \eta_2^{(1)} \end{bmatrix} = \varphi^{(1)}(t_0) - \frac{\alpha_0^{(1)}}{2} - \sum_{i=1}^{M^{(1)}} \alpha_i^{(1)}. \quad (10)$$

*Position connectivity condition on the start-end time of the segments*

Except for the initial (at  $t_0$ ) and final (at  $t_n$ ) conditions, we need the position connectivity condition on the border of the segments. If we have  $n$  segments, we can get  $n - 1$  conditions. That is,

$$\varphi^{(j)}(t_j) = \varphi^{(j+1)}(t_j). \quad (11)$$

And the connectivity condition is

$$\begin{aligned} & \begin{bmatrix} \cosh(\omega_G \Delta t_j) & \sinh(\omega_G \Delta t_j) & -1 & 0 \end{bmatrix} \begin{bmatrix} \eta_1^{(j)} \\ \eta_2^{(j)} \\ \eta_1^{(j+1)} \\ \eta_2^{(j+1)} \end{bmatrix} \\ &= -\frac{\alpha_0^{(j)}}{2} + \frac{\alpha_0^{(j+1)}}{2} - \sum_{i=1}^{M^{(j)}} \left[ \alpha_i^{(j)} \cos\left(i\frac{\pi}{2}\right) + \beta_i^{(j)} \sin\left(i\frac{\pi}{2}\right) \right] \\ &+ \sum_{i=1}^{M^{(j+1)}} \alpha_i^{(j+1)}, \end{aligned} \quad (12)$$

where the interval is  $\Delta t_j = t_j - t_{j-1}$ .

*Velocity connectivity condition*

The velocity connectivity has  $n - 1$  conditions, and those are

$$\dot{\varphi}^{(j)}(t_j) = \dot{\varphi}^{(j+1)}(t_j). \quad (13)$$

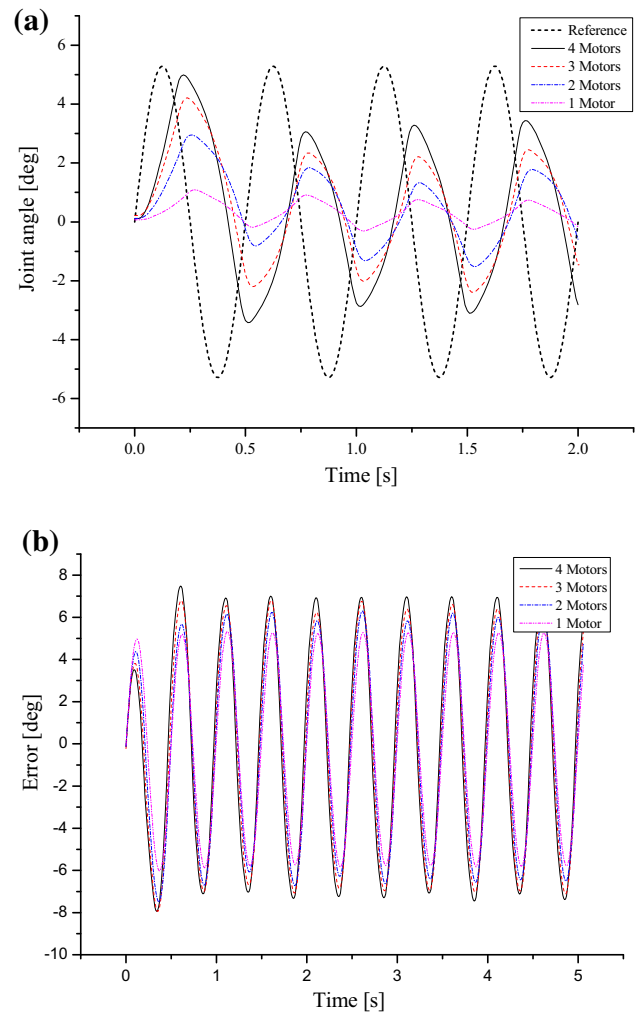


**Fig. 16** Position tracking performance with respect to the number of motors

The connectivity equation from (14) is

$$\begin{aligned} & \begin{bmatrix} \omega_G \sinh(\omega_G \Delta t_j) & \omega_G \cosh(\omega_G \Delta t_j) & 0 & -\omega_G \end{bmatrix} \begin{bmatrix} \eta_1^{(j)} \\ \eta_2^{(j)} \\ \eta_1^{(j+1)} \\ \eta_2^{(j+1)} \end{bmatrix} \\ &= \sum_{i=1}^{M^{(j)}} \left[ (i\omega_0^{(j)}) \left( \alpha_i^{(j)} \sin\left(i\frac{\pi}{2}\right) - \beta_i^{(j)} \cos\left(i\frac{\pi}{2}\right) \right) \right] \\ &+ \sum_{i=1}^{M^{(j+1)}} [i\omega_0^{(j+1)} \beta_i^{(j+1)}]. \end{aligned} \quad (14)$$

*Terminal condition*

When the terminal condition,  $\varphi^{(n)}(t_n)$ , of the CoG at  $t_n$  is given, the equation is derived as follows:

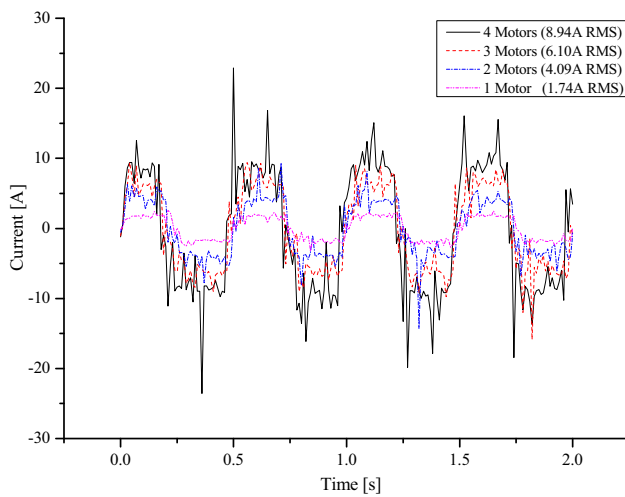


**Fig. 17** Total current consumption of joint with respect to the number of motors

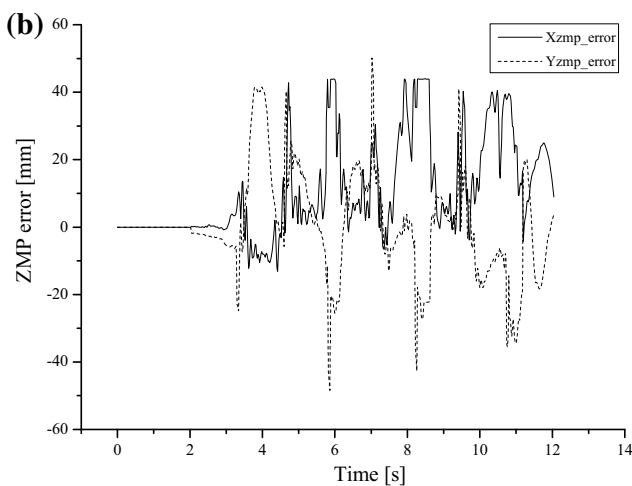
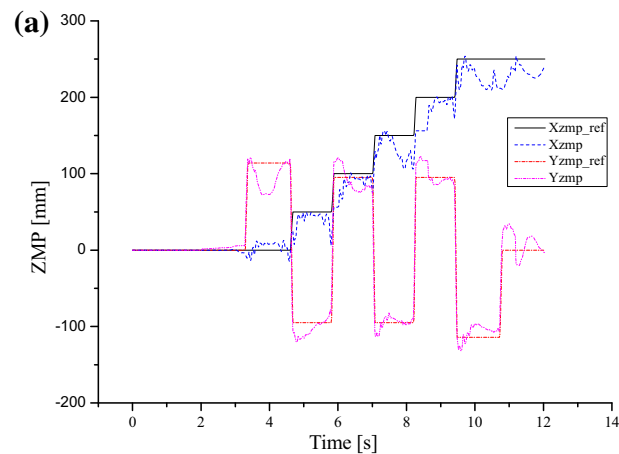


**Fig. 18** Walking experiment results when 1 motor is used on each pitch joint

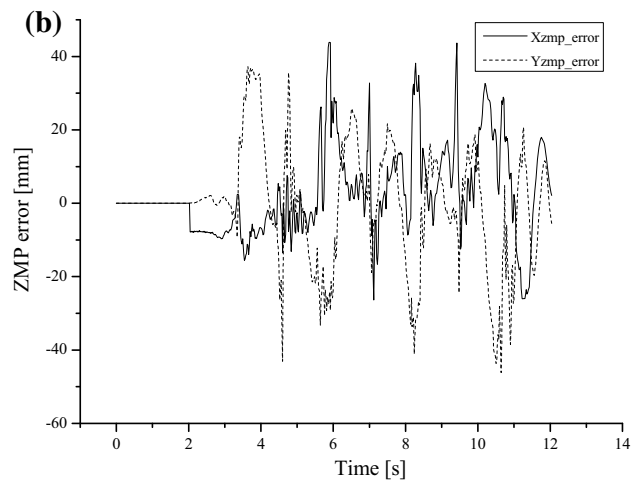
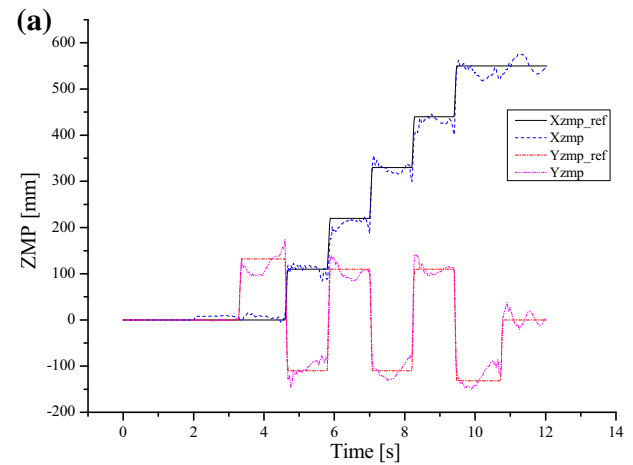


**Fig. 19** Walking experiment results when 4 motors are used on each pitch joint (walking speed 91.7 mm/s)

$$\begin{bmatrix} \cosh(\omega_G \Delta t_n) & \sinh(\omega_G \Delta t_n) \end{bmatrix} \begin{bmatrix} \eta_1^{(n)} \\ \eta_2^{(n)} \end{bmatrix} = \varphi^{(n)}(t_n) - \frac{\alpha_0^{(n)}}{2} - \sum_{i=1}^{M^{(n)}} \left[ \alpha_i^{(n)} \cos\left(i \frac{\pi}{2}\right) + \beta_i^{(n)} \sin\left(i \frac{\pi}{2}\right) \right]. \quad (15)$$

All the equations in this section, including the unknowns ( $\eta$ ) are organized as

$$H\eta = z, \quad (16)$$

where the detailed detail formulas are

$$H = \begin{bmatrix} H_0 & 0 & 0 & 0 & 0 \\ H_1 & \Pi_1 & 0 & 0 & 0 \\ 0 & H_2 & \Pi_2 & 0 & 0 \\ & \ddots & \ddots & \ddots & \\ 0 & 0 & 0 & H_{n-1} & \Pi_{n-1} \\ 0 & 0 & 0 & 0 & H_n \end{bmatrix}, \quad H_0 = \begin{bmatrix} 1 & 0 \end{bmatrix},$$



**Fig. 20** Walking experiment results when 4 motors are used on each pitch joint (walking speed 125 mm/s)



$$H_j = \begin{bmatrix} \cosh(\omega_G \Delta t_j) & \sinh(\omega_G \Delta t_j) \\ \omega_G \sinh(\omega_G \Delta t_j) & \omega_G \cosh(\omega_G \Delta t_j) \end{bmatrix},$$

$$\Pi_j = \begin{bmatrix} -1 & 0 \\ 0 & -\omega_G \end{bmatrix},$$

$$H_m = \begin{bmatrix} \cosh(\omega_G \Delta t_n) & \sinh(\omega_G \Delta t_n) \end{bmatrix},$$

$$\eta = [\eta_1^{(1)} \quad \eta_2^{(1)} \quad \eta_1^{(2)} \quad \eta_2^{(2)} \quad \cdots \quad \eta_1^{(n)} \quad \eta_2^{(n)}]^T,$$

$$z = [z^{(0)} \quad z_1^{(1)} \quad z_2^{(1)} \quad \cdots \quad z_1^{(n-1)} \quad z_2^{(n-1)} \quad z^{(n)}]^T,$$

$$z^{(0)} = \varphi^1(t_0) - \frac{\alpha_0^{(1)}}{2} - \sum_{i=1}^{M^{(1)}} \alpha_i^{(1)},$$

$$z_1^{(j)} = -\frac{\alpha_0^{(j)}}{2} + \frac{\alpha_0^{(j+1)}}{2} - \sum_{i=1}^{M^{(j)}} \left[ \alpha_i^{(j)} \cos\left(i \frac{\pi}{2}\right) + \beta_i^{(j)} \sin\left(i \frac{\pi}{2}\right) \right]$$

$$+ \sum_{i=1}^{M^{(j+1)}} \alpha_i^{(j+1)},$$

$$z_2^{(j)} = \sum_{i=1}^{M^{(j)}} \left[ \left( i \omega_0^{(j)} \right) \left( \alpha_i^{(j)} \sin \left( i \frac{\pi}{2} \right) - \beta_i^{(j)} \cos \left( i \frac{\pi}{2} \right) \right) \right] \\ + \sum_{i=1}^{M^{(j+1)}} [i \omega_0^{(j+1)} \beta_i^{(j+1)}], \text{ and} \\ z^{(n)} = \varphi^{(n)}(t_n) - \frac{\alpha_0^{(n)}}{2} - \sum_{i=1}^{M^{(n)}} \left[ \alpha_i^{(n)} \cos \left( i \frac{\pi}{2} \right) + \beta_i^{(n)} \sin \left( i \frac{\pi}{2} \right) \right].$$

## 8 Experiment

### 8.1 Joint power amplification experiment

An experiment of joint power amplification is carried out to verify that the actuation power is increased with the number of motors on a joint. The test joint is the left leg hip-pitch with an amplitude of  $5.3^\circ$  and a frequency of 2 Hz with a sine wave joint angle: the output side of the harmonic drive. The motors are controlled by a low-gain PD controller. Figures 16 and 17 show the tracking performance and the current consumption with respect to the number of motors. This experiment is conducted under the conditions that the joint swings with a large amount of inertia, a stretched leg, and fast frequency. The conditions are designed to observe the phase delay and amplitude for the reference angle. The tracking performance is in proportion to the applied torque and the torque can be observed by the current consumption of the joint actuator.

The walking performance results are related with the results of Figs. 16 and 17. When the installed motor power and the torque are small, the inertia effects, such as the phase delay, which degrades the performance of tracking amplitude, become dominant and this affects the walking. Even though the high gain servo control of the motor compensates the inertia effects, the current consumption of the joint, which corresponds with the required torque, increases with respect to the amount of control action. When multiple motors are installed in a joint, the required current can be distributed to the motors.

### 8.2 Biped walking experiment

This experiment is carried out for initial verification of the robot hardware design, including mechanical, electrical, and system integration. The walking action of the robot is realized as shown in Figs. 18, 19, and 20 with the experiment conditions in Table 3. Simple algorithms for walking, such as trajectory generation, landing detection, and a low-level ZMP controller, are implemented on the experiments [20–22]. With 4 motors on each leg pitch joint (hip, knee, and ankle), walking can be realized in all conditions of Table 3, but the walking has limited performance (maximum walking

**Table 3** Biped walking experiment conditions

Conditions	Figure 18	Figure 19	Figure 20
Number of motors on pitch joints	1	4	4
Step length (mm)	50	110	100
Step time (s)	1.2	1.2	0.8
Swing foot height (mm)	70	70	50
Walking speed (mm/s)	41.7	91.7	125

speed: 41.7 mm/s) when 1 motor is used. When 4 motors are used, the X direction ZMP errors (mean and standard deviation value) are lower with the similar Y direction ZMP errors, even though the step length is more than twice than the case of 1 motor used.

With these experiments, the designed robot system realized biped walking with multiple motors in each joint. The walking performance will be upgraded with the future implementation of a dynamic walking algorithm.

## 9 Conclusion

Mechanical and electrical design result is presented for the biped humanoid robot which has multiple motors on each joint of the lower body. Sensor system and system integration approach are explained including software environment. The walking realization experimental results are also presented based on the stable walking trajectory generation method, which uses SIPM.

The design results of a humanoid that has multiple motors in a leg joint are reported. The concept of torque amplification of the joint actuator is presented using a design parameter, P/W. The performance of the actuator is evaluated experimentally with the number of motors installed on a joint. The torque amplification is verified by an experiment. And the experimental data are presented which is about the effect of multiple motors to the walking performance. The joint current consumption increases with the number of motors. The tracking performance is improved with the consumed current, which is proportional to the joint torque. The increased joint torque accordingly improves the joint position tracking control, and the walking performance is enhanced together with the walking speed. With the proposed design approach, power amplification of each joint can be realized without major change of mechanical design of the robot.

Simple control algorithms to realize stable walking are implemented, but a detailed explanation of these algorithms is outside the scope of this paper. They are partially adopted

from earlier research [20–22]. A more advanced control scheme will be realized in the future.

**Acknowledgments** The present research has been conducted under support from a research grant of Kwangwoon University in 2015, the MOTIE (Ministry of Trade, Industry and Energy), and the KIAT (Korea Institute for Advancement of Technology) through the Industry Convergence/Connected for Creative Robot Human Resource Development (N0001126).

## References

- Asano F, Yamakita M, Kamamichi N, Luo Z (2004) A novel gait generation for biped walking robots based on mechanical energy constraint. *IEEE Trans Robot Autom* 20(3):565–573
- Lohmeier S (2010) Design and realization of a humanoid robot for fast and autonomous bipedal locomotion. PhD thesis, Dipl.-Ing. Univ., Technische Universität München, Munich
- Ogura Y, Aikawa H, Lim H-O, Takanishi A (2004) Development of a human-like walking robot having two 7-DOF legs and a 2-DOF waist. In: *Proceedings of the IEEE international conference on robotics and automation (ICRA)*, pp 134–139
- Takenaka T, Matsumoto T, Yoshiike T, Shirokura S (2009) Real time motion generation and control for biped robot—2nd report: running gait pattern generation. In: *Proceedings of the IEEE/RSJ international conference on intelligent robots and systems (IROS)*, pp 1092–1099
- Kaneko K, Harada K, Kanehiro F, Miyamori G, Akachi K (2008) Humanoid robot HRP-3. In: *Presented at Proceedings of the IEEE/RSJ international conference on intelligent robots and systems (IROS)*, pp 2471–2478
- Yu Z, Huang Q, Ma G, Chen X, Zhang W, Li J, Gao J (2014) Design and development of the humanoid robot BHR-5. *Adv Mech Eng* 852937:1–11
- Kwon W, Kim H, Park J, Roh C, Lee J, Park J, Kim W, Roh K (2007) Biped humanoid robot Mahru III. In: *Proceedings of the IEEE-RAS international conference on humanoid robots*, pp 583–588
- Kim J, Lee Y, Kwon S, Seo K, Kwak H, Lee H, Roh K (2012) Development of the lower limbs for a humanoid robot. In: *IEEE/RSJ international conference on intelligent robots and systems*, pp 4000–4005
- Nozawa S, Urata J, Nakaoka T, Kobayashi K, Nakanishi Y, Okada K, Inaba M, Ito Y (2014) Development and verification of life-size humanoid with high-output actuation system. In: *IEEE international conference on robotics and automation*, pp 3433–3438
- Park I-W, Kim J-Y, Lee J, Oh J-H (2007) Mechanical design of the humanoid robot platform. *HUBO. Adv Robot* 21(11):1305–1322
- Heo J-W, Lee I-H, Oh J-H (2012) Development of humanoid robots in HUBO Laboratory, KAIST. *J Robot Soc Jpn* 30(4):367–371
- Cho B-K, Park S-S, Oh J-H (2009) Controllers for running in the humanoid robot, HUBO. In: *Proceedings of the IEEE-RAS international conference on humanoid robots*, pp 385–390
- <http://www.hds.co.jp/english/products/lineup/hd/> 4 Aug 2015
- <http://www.maxonmotor.com/maxon/view/content/products> 4 Aug 2015
- Semwal V-B, Katiyar S-A, Chakraborty R, Nandi G-C (2015) Biologically-inspired push recovery capable bipedal locomotion modeling through hybrid automata. *Robot Auton Syst* 70:181–190
- Semwal V-B, Nandi G-C (2015) Developing toward a computational model for bipedal push recovery—a brief. *IEEE Sens J* 15(4):2021–2022
- Park I-W, Kim J-Y (2014) Biomimetic walking trajectory generation of humanoid robot on an inclined surface using Fourier series. *J Nanosci Nanotechnol* 14(1):1–7
- Harada K, Kajita S, Kanehiro F, Fujiwara K, Kaneko K, Yokoi K, Hirukawa H (2004) Real-time planning of humanoid robot's gait for force controlled manipulation. In: *IEEE international conference on robotics and automation*, pp 616–622
- Sugihara T, Nakamura Y (2005) A fast online gait planning with boundary condition relaxation for humanoid robots. In: *IEEE international conference on robotics and automation*, pp 305–310
- Park I-W, Kim J-Y, Lee J, Oh J-H (2006) Online free walking trajectory generation for biped humanoid robot KHR-3 (HUBO). In: *Proceedings of the IEEE international conference on robotics and automation*, pp 1231–1236
- Park I-W, Kim J-Y, Lee J, Oh J-H (2008) Online walking pattern generation and its application to a biped humanoid robot-KHR-3(HUBO). *Adv Robot* 22(2–3):159–190
- Kim J-Y, Park I-W, Oh JH (2006) Experimental realization of dynamic walking of biped humanoid robot KHR-2 using ZMP feedback and inertial measurement. *Adv Robot* 20(6):707–736
- Kim J-H, Park I-W, Oh JH (2002) Design of lower limbs for a humanoid biped robot. *Int J Hum Friendly Welf Robot Syst* 2(4):5–10